Title page

Title: Cracking behavior of CA-UHPC overlay in steel-CA-UHPC composite bridge deck: Flexural tension test and restrained shrinkage effect

Author names: Zhanchong Shi[a,b], Chen Lin[b], Qingtian Su[a,c*], Liberato Ferrara[d]

Affiliations: [a]Department of Bridge Engineering, Tongji University, Shanghai 200092, China;

[b]Department of Structural Engineering, Norwegian University of Science and Technology, Richard Birkelandsvei 1A, 7034 Trondheim, Norway

[c]Shanghai Engineering Research Center of High Performance Composite Bridges, Shanghai 200092, China;

[d]Department of Civil and Environmental Engineering, Politecnico di Milano, Piazza Leonardo DaVinci 32, 20133 Milan, Italy

Corresponding authors: Qingtian Su (E-mail: sqt@tongji.edu.cn)

Address: 1239 Siping Road**,** Tongji University, Shanghai 200092, China.

Cracking behavior of CA-UHPC overlay in steel-CA-UHPC composite bridge deck: Flexural tension test and restrained shrinkage effect

Zhanchong Shi[a,b], Chen Lin[a], Qingtian Su[a,c*], Liberato Ferrara[d]

[a]*Department of Bridge Engineering, Tongji University, Shanghai 200092, China*

[b]*Department of Structural Engineering, Norwegian University of Science and Technology, Richard Birkelandsvei 1A, 7034 Trondheim, Norway*

[c]*Shanghai Engineering Research Center of High Performance Composite Bridges, Shanghai 200092, China*

[d]*Department of Civil and Environmental Engineering, Politecnico di Milano, Piazza Leonardo DaVinci 32, 20133 Milan, Italy*

ABSTRACT

Coarse Aggregate Ultra-High Performance Concrete (CA-UHPC) has emerged as a promising alternative UHPC material for steel-UHPC composite decks due to its reduced autogenous shrinkage. The cracking performance of CA-UHPC overlay is of interest to ensure the composite deck stiffness. To this end, flexural-tension tests on the composite decks were conducted to explore the effects of reinforcement ratios, concrete covers, concrete types (CA-UHPC vs. normal concrete), and loading nature (monotonic vs. cyclic). Test observations indicate that the restrained shrinkage effect leads to premature cracking of the CA-UHPC overlay under external loads. Increasing reinforcement ratios or reducing concrete covers helps to control maximum crack widths. When reinforcement ratios exceed 2.1%, maximum crack widths of CA-UHPC overlay remain below 0.2 mm. Unlike normal concrete, steel rebars embedded in CA-UHPC overlays do not yield. Limited cyclic tension has a negligible impact on the cracking response. Moreover, a theoretical analysis based on the Trost-Bazant-algebraic-equations was conducted to understand the restrained shrinkage-induced internal force redistribution. Finally, an empirical model between the proposed restrained degree and steel-CA-UHPC bending stiffness ratio was developed to predict the restrained tensile stresses and the initial cracking loads. This study provides deeper insights into the cracking behavior of CA-UHPC overlay under various conditions, contributing to the optimization of such composite decks.

Keywords: CA-UHPC, steel-UHPC composite deck, crack pattern, restrained shrinkage effect, restrained tensile stress.

1. Introduction

Orthotropic steel deck (OSD) systems, as plotted in Fig.1(a), consisting of a OSD (including steel deck plate, closed longitudinal ribs, and crossbeams) and asphalt wearing course, have been widely used in large-span bridges throughout the world, owing to the higher load-bearing capacity, lighter self-weight, and easier installation [1]. Due to the complicated welded connections and insufficient local deck stiffness [2,3], fatigue cracking at the welds [4,5] and wearing of asphalt surfacing [2,6] have become interest of concern

worldwide since the 1970s. To tackle these challenges, a thin rebar-reinforced ultra-high performance concrete (UHPC) overlay (35~80 mm) has been introduced into the OSD in order to stiffen the deck system. The UHPC overlay is connected to the steel deck plate by using epoxy-based adhesive [7–9] or welded studs [10–12], and the deck system is usually named steel-UHPC composite bridge deck, as shown in Fig.1(b).

UHPC, as a nowadays "state-of-art" category of fiber-reinforced cementitious composites, is typically characterized by [13]: (1) compressive strength higher than 120 MPa; (2) elastic modulus greater than 40 GPa; (3) sustained post-cracking tensile strength larger than 5 MPa; and (4) a disconnected pore structure that significantly reduces permeability and thus enhances durability. However, an extremely low water/binder ratio (less than 0.2) and a high amount of fine reactive admixtures lead to a significantly high early-age autogenous shrinkage for UHPC [14–16]. This will induce restrained tensile stress and even tensile cracking of UHPC overlay in the composite deck system at early ages, resulting in a decreased stiffening effect on the OSD. Therefore, reducing the early-age shrinkage of UHPC has become a major concern when used in the composite deck.

So far, the steam-curing strategy [16,17] and the use of shrinkage-reducing admixture [14,18,19] have been investigated to identify the shrinkage-reducing effect. Another alternative solution is to add coarse aggregates to mitigate the cement paste shrinkage [20–22]. The UHPC containing coarse aggregates is denoted as CA-UHPC to distinguish it from the conventional UHPC. Moreover, compared with UHPC without coarse aggregates, CA-UHPC has demonstrated enhanced compressive strength and elastic modulus, anyway accompanied by a reduced tensile performance [22–25], especially in terms of tensile ductility and ultimate strain capacity as well as in the ability to achieve tensile strain-hardening behavior.

When CA-UHPC is used as the overlay material in the composite deck system, cracking concerns are of the utmost importance. On one hand, as shown in Fig.1(b), under repeated vehicle wheel loads, the concrete overlay above the crossbeams is inevitably subjected to tension, leading to a significant external load-induced cracking potential. On the other hand, though characterized by reduced autogenous shrinkage, the free shrinkage of the CA-UHPC overlay will be restrained by the steel rebars and by the OSD as a whole, resulting in internal tensile stresses and cracking risks. However, the application of CA-UHPC in the composite deck is still in the preliminary stage [26]. To the best of the authors' knowledge, insights into both the cracking performance and cracking potential of the CA-UHPC overlay have not been investigated and reported. This has created a knowledge gap in the engineering practice worth further investigation at both the material and macro-structural scale.

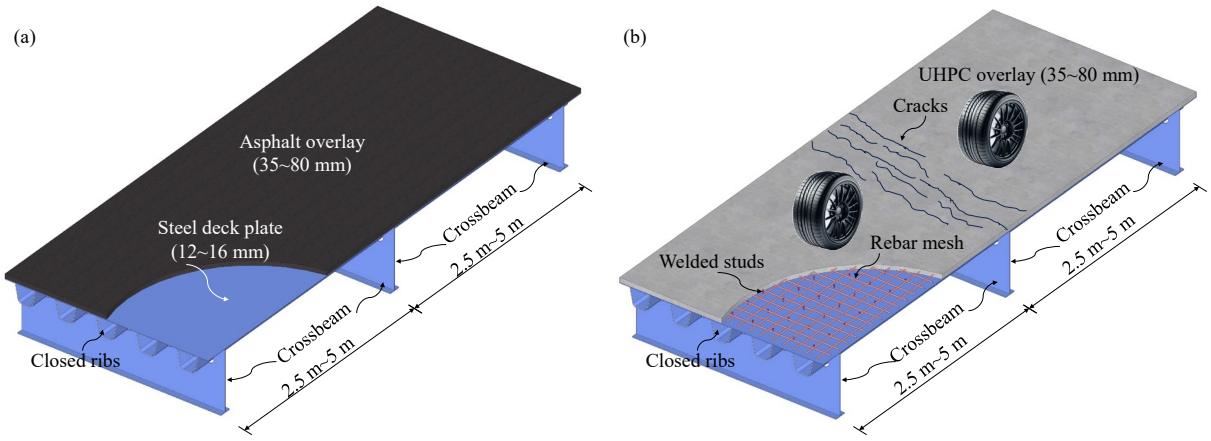

Fig.1. Bridge deck system: (a) OSD; and (b) steel-UHPC composite deck.

Therefore, in the framework described above, this study aims to clarify the cracking performance and restrained shrinkage-induced cracking potential of the CA-UHPC overlay in the composite deck. Full-scale flexural tension tests were conducted to identify the influence of reinforcement ratios, concrete covers, concrete types, and load nature (monotonic vs cyclic) on the crack patterns and crack widths of the CA-UHPC overlay. A theoretical analysis based on the Trost-Bazant-algebraic-equations was performed to clarify the restrained shrinkage effects and validated with experimental measurements. Finally, a restrained degree parameter was proposed to quantify the restrained shrinkage effect and a restrained shrinkage model was developed to predict the restrained tensile stresses and the initial cracking loads of the composite deck.

2. Experimental program

2.1 Test design and conduction

2.1.1 Specimen design

Eight steel-concrete composite deck specimens with a single rib were designed and fabricated. Fig.2 shows the structural details of the benchmark specimen. All specimens had a total length of 4800 mm, a width of 720 mm, and a depth of 392 mm, consisting of an 80-mm thick reinforced concrete/CA-UHPC overlay and single-rib-stiffened steel plate. The steel plate and the concrete overlay were connected by short welded studs (diameter of 13 mm and a post-weld height of 45 mm). The longitudinal and transverse spacings of the welded studs were 360 mm and 280 mm, respectively. In the concrete overlay, 16-mm diameter HRB400 steel rebars were arranged in a mesh, arranged with longitudinal rebars on the top and transverse rebars at the bottom, with a longitudinal spacing of 120 mm.

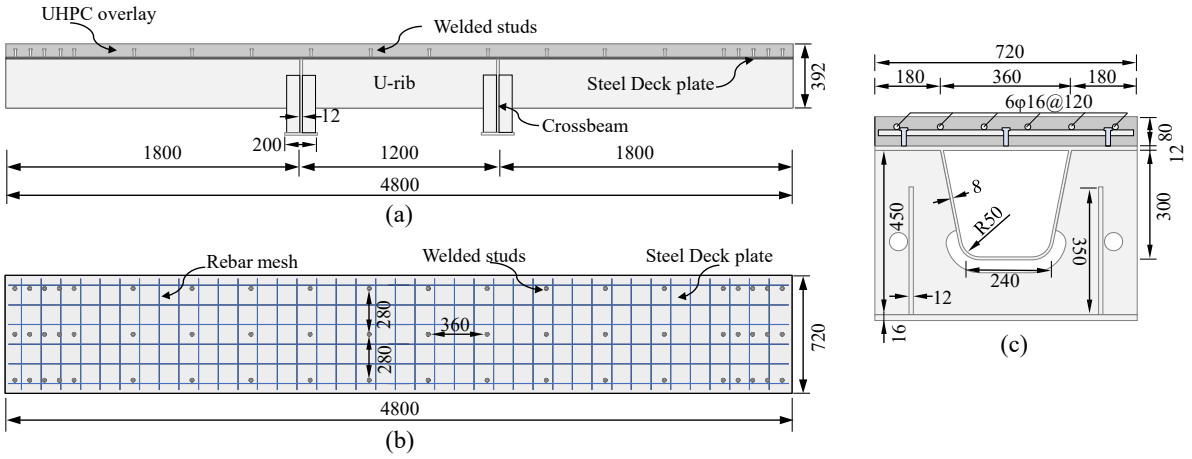

Fig.2. Specimen details (unit: mm): (a) basic sizes; (b) welded studs and steel rebar arrangements; and (c) cross-section at the crossbeam location.

Table 1 lists the basic information of the designed specimens, where specimen SN-3 served as the benchmark. The studied parameters are as follows:

(1) Reinforcement ratios ρ_s: 0 to 3.1%. This value was calculated as the ratio of the longitudinal steel rebar area to the gross cross-sectional area of the concrete overlay. For specimen SN-1 with a reinforcement ratio of 0, no transverse rebars were provided. The transverse rebar arrangement for the remaining specimens was the same with a spacing of 120 mm.

(2) Concrete covers c: 10 mm, 20 mm, and 30 mm, which was defined as the clear distance from the longitudinal steel rebar to the concrete top surface.

(3) Concrete types, comparing the cracking behavior between CA-UHPC and normal concrete (NC).

(4) Load nature, identifying the influence of monotonic vs. cyclic loadings on the cracking response of CA-UHPC overlay.

Table 1. Specimen design.

No.	Parameters	Rebar quantity	ρ_s	c [mm]	Loading methods	Concrete types
SN-1	reinforcement ratios ρ_s	0	0	—	monotonic	CA-UHPC
SN-2		3	1.1%	20		CA-UHPC
SN-3		6	2.1%	20		CA-UHPC
SN-4		9	3.1%	20		CA-UHPC
SN-5	concrete covers c	6	2.1%	10		CA-UHPC
SN-6		6	2.1%	30		CA-UHPC
SN-7	concrete types	6	2.1%	20		NC
SN-8	loading methods	6	2.1%	20	cyclic	CA-UHPC

2.1.2 Specimen preparation and curing

Fig.3 shows the four main fabricating procedures for the specimens. To minimize water evaporation and prevent early-age cracking in the concrete overlay, the concrete overlay was covered with film as soon as after leveling it. Then, the specimens were cured for 37 days in

an outdoor environment with an average temperature of 12~18°C and an average relative humidity of 72% (mid-November in Shanghai, China).

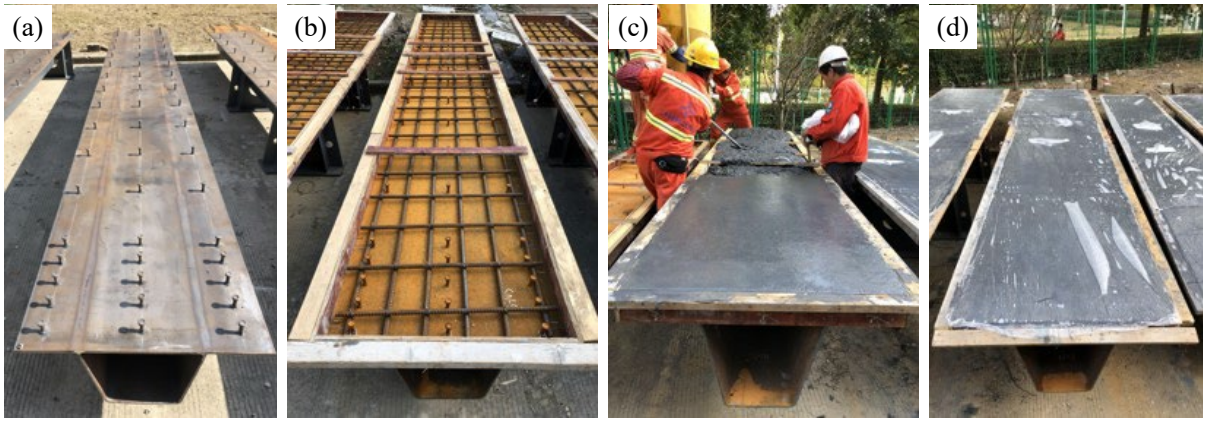

Fig.3. Specimen fabrication: (a) making of OSD and welded studs； (b) rebar tying and formwork erection; (c) concrete casting; and (d) concrete curing.

2.1.3 Test setup and loading protocols

The crack initiation and propagation of the CA-UHPC overlay are the major concerns of this study. To facilitate the crack observation, the specimens were designed into a 4-point bending form, which consisted of a 1200-mm long central pure bending zone (for crack monitoring) and two 1800-mm long cantilever zones (for test loading).

Fig.4(a) shows the 4-point bending test setup. The specimens were placed on a support pedestal. Vertical loads were applied to the specimens using an MTS electro-hydraulic servo loading system, which was able to enforce the force to two loading points simultaneously.

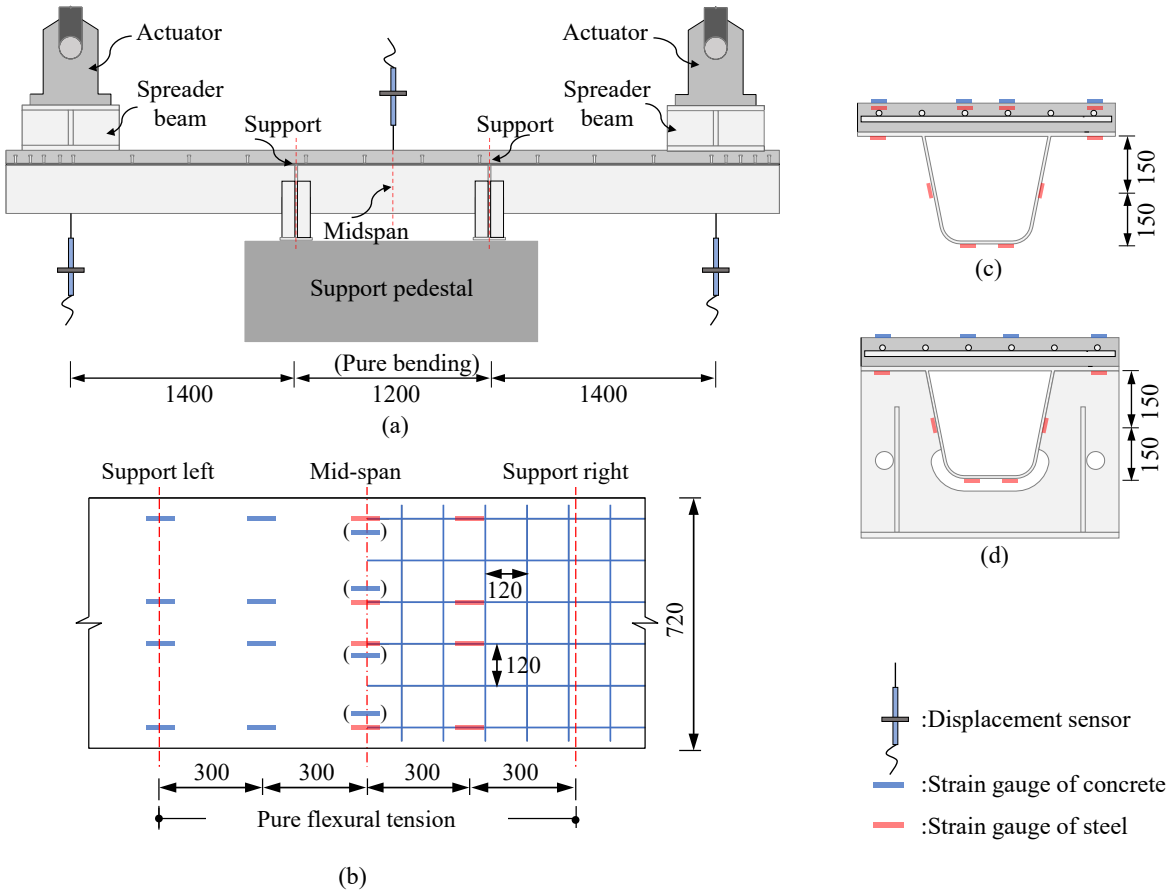

Fig.4. Test setup and measuring points arrangement (unit: mm): (a) test setup and displacement sensor arrangement; (b) measuring points for concrete overlay and longitudinal rebars; (c) measuring points at mid-span cross-section; (d) measuring points at the support cross-section.

The measuring points are illustrated in Fig.4(a) to (d). The deflection at the loading-point cross-section was monitored through displacement sensors placed at the U-rib bottom. Longitudinal strain developments were measured using strain gauges placed on the surfaces of the concrete overlay, steel rebars, steel deck plate, U-rib web, and U-rib bottom at the mid-span cross-section as well as at the support cross-section. The transverse locations of the rebar strain gauges were aligned with those of the concrete strain gauges.

Fig.5 illustrates the loading protocols. The monotonic loading consisted of two stages: (1) Preloading was performed using force-controlled loading up to 20 kN, followed by unloading. This stage was employed to verify the proper functioning of the testing equipment. (2) "Actual" loading: Firstly, force-controlled loading was applied at a rate of 10 kN per increment until yielding was reached at the U-rib bottom, identified through the thereby positioned strain gauges. Subsequently, the control was shifted to displacement, and vertical deflection of the loading actuator was applied at a rate of 0.1 mm/s until ultimate failure.

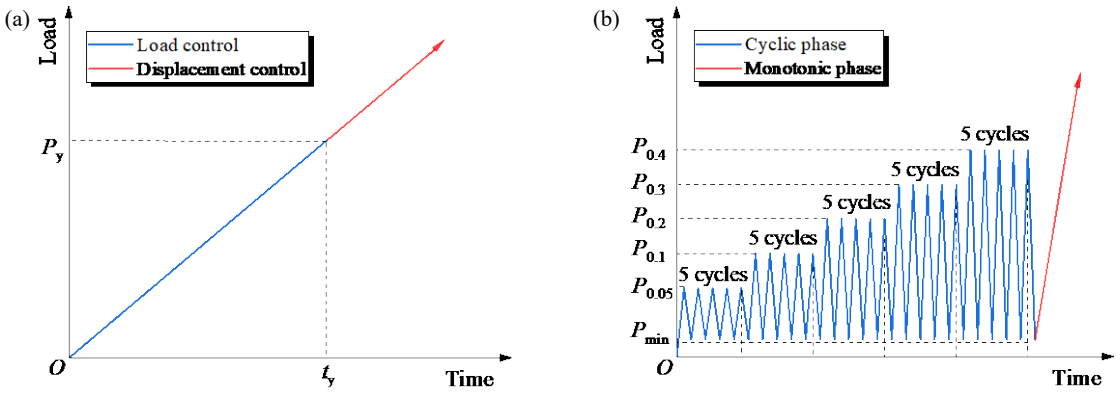

Fig.5. Loading protocols: (a) monotonic; and (b) cyclic.

As for the cyclic loading protocol, the preloading stage was identical to the monotonic loading. During the actual loading stage, force-controlled loading was applied up to $P_{0.05}$, which was defined as the force at a maximum concrete crack width of 0.05 mm. Subsequently, the load was decreased down 5 kN and then increased back to $P_{0.05}$ for a total of 4 cycles. The loading-unloading cycles were similarly repeated 5 times each for maximum crack widths of 0.1 mm, 0.2 mm, 0.3 mm, and 0.4 mm. Then, force-controlled monotonic loading was applied until the yielding at the U-rib. Finally, the loading was switched to a displacement-controlled type until ultimate failure.

After each loading increment was completed, the crack developments of the concrete overlay at the pure bending zone were visually observed and recorded. Crack widths were measured using crack observation devices with an accuracy of 0.01 mm.

2.1.4 Material properties characterization

As listed in Table 2, the CA-UHPC consists of reactive powders, river sand, basalt aggregates (with a maximum particle size equal to 8 mm), water, superplasticizer, and steel fibers. The steel fiber reinforcement with a total volume fraction of 2.5% consisted of straight fibers (length of 13 mm and diameter of 0.2 mm, dosage of 1%) and hooked-end ones (length of 20 mm and diameter of 0.25 mm, dosage of 1.5%). The NC contained gravel of 1080 kg/m^3, sand of 780 kg/m^3, cement of 450 kg/m^3, water of 154 kg/m^3, and water reducer of 4.5 kg/m^3.

Axial tension tests on 50 mm×100 mm×560 mm dog-bone-shaped specimens [27], elastic modulus tests (on prism specimens 100 mm×100 mm×300 mm for CA-UHPC and 150 mm×150 mm×300 mm for NC), compressive strength tests (same specimen as for elastic modulus test), and 4-point bending test on 100 mm×100 mm×400 mm prism specimens (only for CA-UHPC) for concrete, were conducted. The obtained average mechanical properties of three identical samples are summarized in Table 3. All these material specimens were cured for 28 days under the same outdoor environment as the composite deck specimens. The first author has developed the tensile constitutive model of CA-UHPC [27], as plotted in Fig.6(a), which exhibits strain softening upon reaching the elastic tensile strength.

Table 2. Material compositions of 1 m^3 CA-UHPC (unit: kg).

Reactive	Sand	Basalt	Steel fibers	Superplasticizer	Water

powder		aggregates	straight	hooked		
1173	616	472	89	109	25.7	138

Table 3. Mechanical properties of concrete (unit: MPa).

Concrete	E_c	f_c	$f_{c,cu}$	f_{ct}	$f_{cr,fl}$	$f_{ct,fl}$
NC	36633	49	62	2.59	—	—
CA-UHPC	48733	96	108	7.45	11.53	22.38

Notes：$E_c, f_c, f_{c,cu}, f_{ct}, f_{cr,fl}, f_{ct,fl}$ denote elastic modulus, axial compressive strength (on prisms), cubic compressive strength, tensile strength, first cracking strength under flexural tension; and flexural tensile strength, respectively.

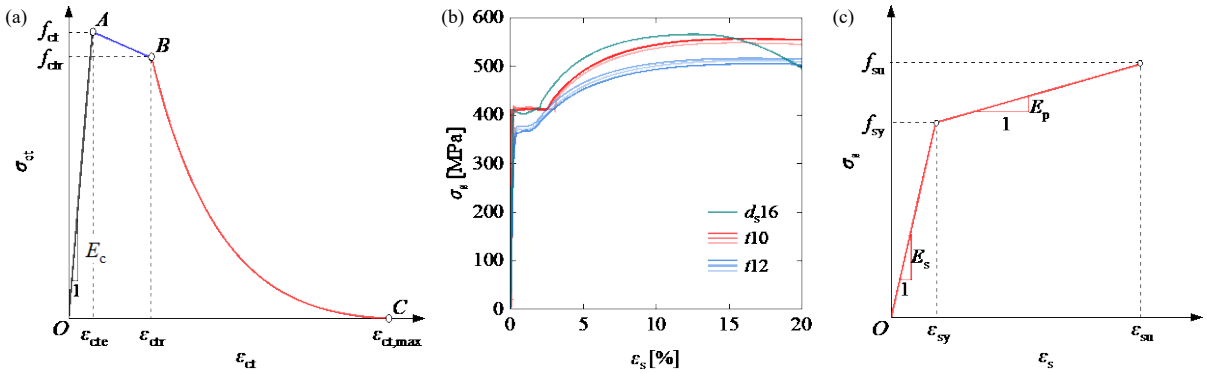

Fig.6. Axial tensile constitutive models: (a) of CA-UHPC [28]; (b) tensile stress-strain response of steel rebar and steel plate; and (c) simplified tension constitutive model of steel rebar and steel plate.

The steel plate and steel rebar were made of Q345 and HRB400, respectively. The tensile stress-strain curves of the steel plate and steel rebar are shown in Fig.6(b), and the simplified bilinear constitutive model is plotted in Fig.6(c). The characteristic mechanical properties of the bilinear constitutive model are summarized in Table 4.

Table 4. Mechanical properties of steel.

Material	t or d_s [mm]	f_{sy} [MPa]	f_{su} [MPa]	ε_{sy} [×10^{-6}]	ε_{su} [×10^{-6}]	E_s [MPa]	E_p [MPa]
Q345	8	411	554	1957	158269	209877	917
	12	370	511	1761	170963	209530	837
HRB400	16	407	566	1958	124925	207880	1296

Note: t is thickness, d_s is diameter.

2.2 Test results and analysis

2.2.1 Flexural-tension response and failure modes

Fig.7(a)~(e) shows the flexural-tension response of the specimens, where P represents the load applied to one loading point, δ denotes the measured deflection from the

displacement sensor at the loading-point U-rib bottom. Overall, all specimens featured similar flexural-tension responses no matter of different reinforcement ratios, concrete covers, concrete types, and loading methods.

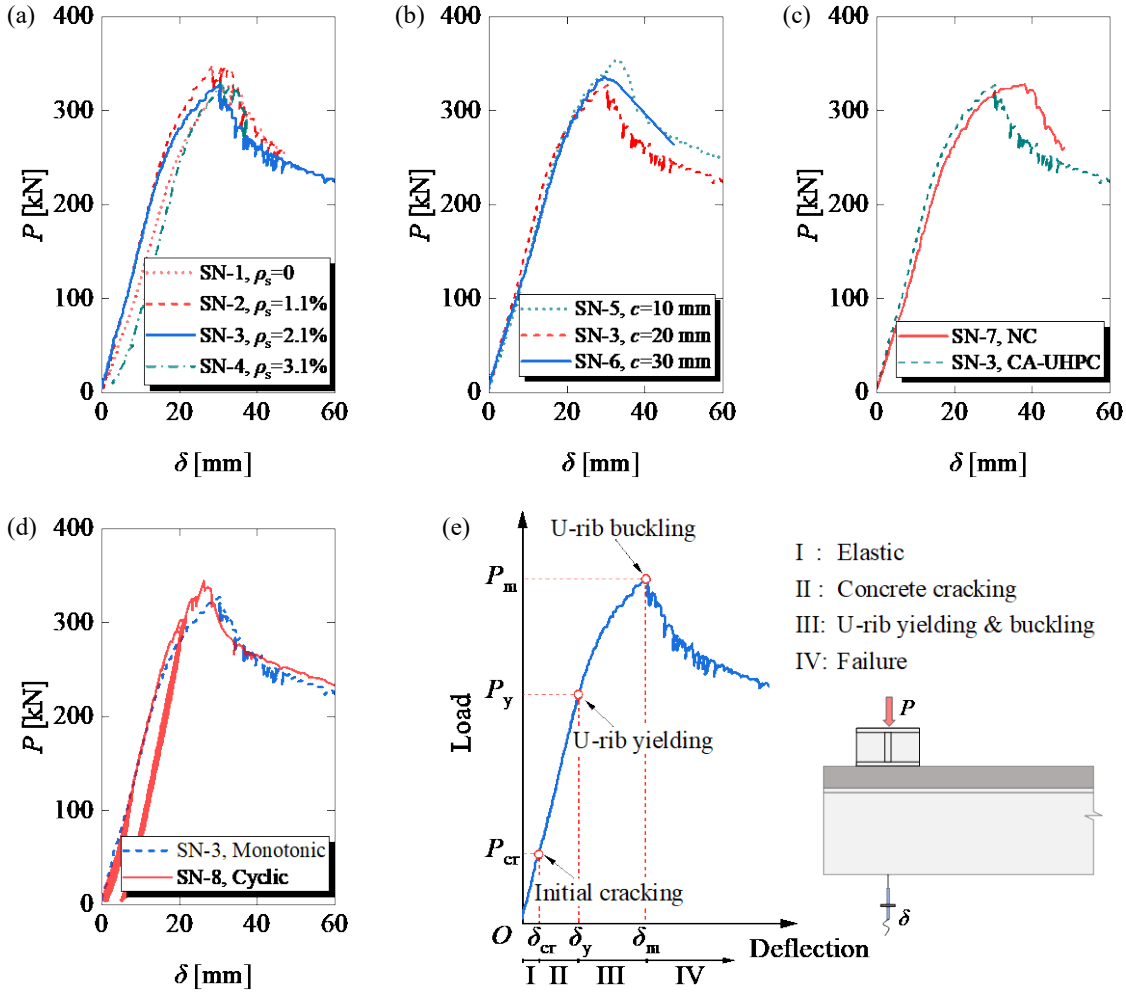

Fig.7. Load-deflection responses: (a) reinforcement ratios; (b) concrete covers; (c) concrete types; (d) loading methods; and (e) schematic flexural-tension response.

Fig.7(e) presents a schematic flexural-tension response of the steel-concrete composite deck specimens, which can be divided into four stages:

Stage I: Elastic stage, which ends with the initial cracking of concrete overlay.

Stage II: Concrete cracking stage. With the increase in external loads, the crack numbers increased and the crack widths widened. This stage concludes with the compressive yielding at the U-rib bottom plate. Despite the crack-induced weakened tension contribution of the concrete overlay, the load-deflection curve still exhibited a linear response owing to the dominant bending stiffness contributed by the steel elements. The compressive yielding of the U-rib bottom plate corresponded to the linear deviation point in the load-deflection curve.

Stage III: U-rib yielding and buckling stage. With external loads increased, the yielding in the U-rib gradually progressed from the bottom plate to the web plate. Finally, local buckling of the U-rib bottom plate developed at the support cross-section. This phenomenon

was similar to the experimental results of the relevant existing study [28] on steel-UHPC composite decks. During this stage, the crack widths of concrete overlay further developed, while the crack numbers remained relatively stable.

Stage IV: Post-peak failure stage. The local buckling of the U-rib was continuously deformed, and a localized crack developed in the concrete overlay at the support cross-section. The ultimate failure modes are presented in Fig.8.

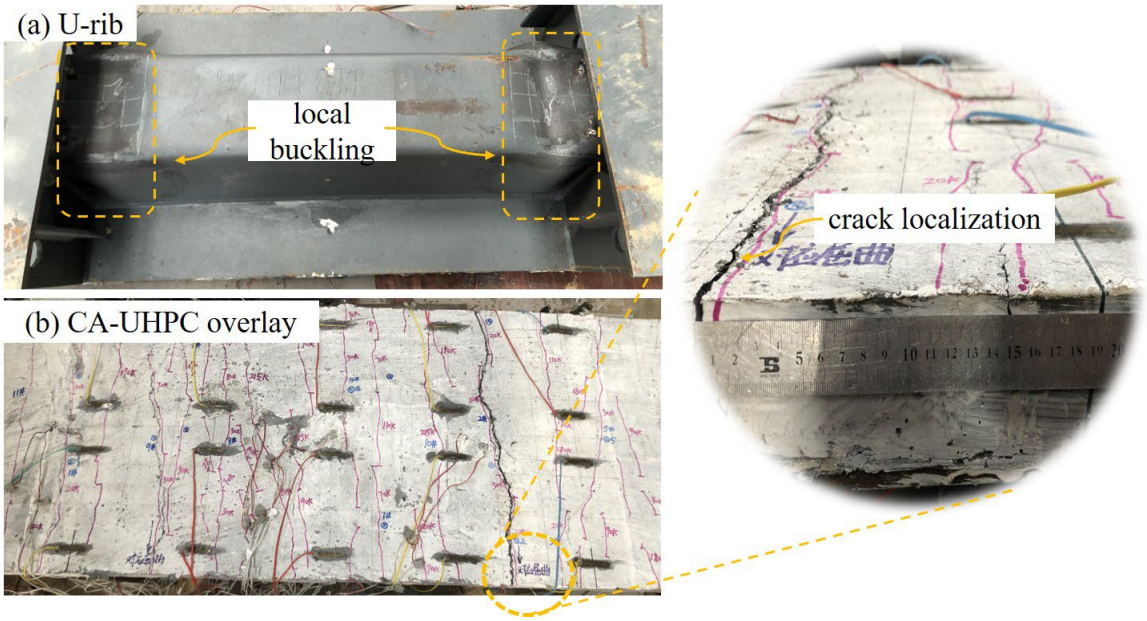

Fig.8. Ultimate failure modes: (a) local buckling of U-rib; and (b) crack localization at concrete overlay.

2.2.2 Characteristic loads and deflections

Table 7 summarizes loads and deflections at characteristic points, including the initial cracking point (δ_{cr}, P_{cr}), the yielding point (δ_y, P_y), and the peak point (δ_m, P_m).

Table 7. Characteristic loads and deflections (load unit: kN, deflection unit: mm).

No.	Mark	Initial cracking			Yielding		Peak	
		P_{cr}	$P_{cr,theo}$	δ_{cr}	P_y	δ_y	P_m	δ_m
SN-1	ρ_s0-/-U-M	20	68	1.75	211	16.23	327	32.71
SN-2	ρ_s1.1%-c20-U-M	15	70	1.04	233	14.20	349	28.56
SN-3	ρ_s2.1%-c20-U-M	20	72	0.92	196	12.15	327	30.43
SN-4	ρ_s3.1%-c20-U-M	40	74	1.30	246	15.21	347	29.96
SN-5	ρ_s2.1%-c10-U-M	30	72	1.86	210	14.33	353	32.56
SN-6	ρ_s2.1%-c30-U-M	20	71	1.05	224	12.99	337	27.99
SN-7	ρ_s2.1%-c30-N-M	35	29	2.25	220	15.31	328	38.06
SN-8	ρ_s2.1%-c20-U-C	30	72	2.31	231	14.16	345	26.26

Notes: ρ_s0/1.1%/2.1%/3.1% represent the longitudinal reinforcement ratio of 0, 1.1%, 2.1%, and 3.1%, respectively; c10/20/30 represent the concrete cover of 10 mm, 20 mm, and 30 mm, respectively; U/N represent CA-UHPC and NC, respectively; M/C represent monotonic

loading and cyclic loading, respectively.

It can be observed that all the specimens had approximately the same yielding load and peak load. The experimental cracking load P_{cr} was further compared with the theoretical cracking load $P_{cr,theo}$. The experimental cracking load P_{cr} was determined by visually identifying the initial cracking of the concrete overlay. At this stage, the crack width was estimated to be approximately 0.02 mm, a dimension beyond the accurate measurement capability of the crack observation device. By assuming full steel-concrete composite action, the theoretical cracking load $P_{cr,theo}$ was derived from the uncracked transformed composite section. This was achieved at the point where the tensile edge of the concrete overlay reached its tensile strength, as depicted in Fig.9 and defined by Eq.s(1) and Eq.(2).

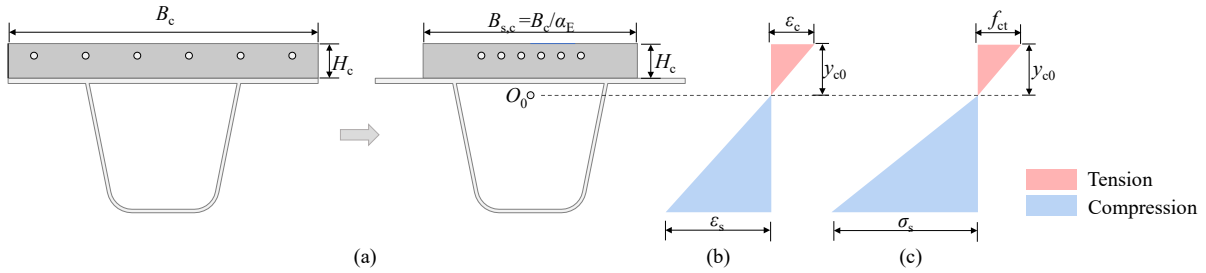

Fig.9. (a) Schematic diagram of the transformed composite section; (b) strain distribution; and (c) stress distribution.

$$B_{s,c}=\frac{B_c}{\alpha_E} \tag{1}$$

where B_c is the width of the concrete overlay; $B_{s,c}$ is the transformed section width of the concrete overlay into steel; α_E is the elastic modulus ratio of steel to concrete, $\alpha_E=E_s/E_c$.

$$P_{cr,Theo}=\frac{f_{ct}I_0\alpha_E}{L_0 y_{c0}} \tag{2}$$

where I_0 is the moment of inertia of the transformed composite section; y_{c0} is the vertical distance from the tensile edge of the concrete overlay to the centroid of the transformed composite section; L_0 is the distance from the cantilever loading point to the corresponding support point.

In contrast, the experimental cracking load observed in the NC specimen was close to the theoretical value. However, for the CA-UHPC specimens, the experimental cracking loads were notably below the theoretical predictions. This discrepancy can be attributed to the greater early-age autogenous shrinkage of CA-UHPC compared to NC. As a result, the shrinkage of CA-UHPC was restrained by the presence of steel elements, resulting in the development of tensile stress within the CA-UHPC overlay and subsequent premature cracking. A detailed mechanism analysis will be further elaborated in the following section.

2.2.3 Load-strain curves and strain distributions

Fig.10 shows the load-strain curves for the representative specimens, the benchmark specimen SN-3, the NC specimen SN-7, and the cyclic loading specimen SN-8. The strain measuring points for concrete were selected from undamaged strain gauges, while the strain values for steel rebar and steel plates were the average value of strain gauges at the same section depth.

Specimens SN-3, SN-7, and SN-8 had the same reinforcement ratio (ρ_s = 2.1%) and concrete cover (c = 20 mm). It can be observed that:

(1) Overall, the steel deck plate, steel rebar, and concrete overlay were subjected to tension, while the U-rib side was at compression. Additionally, the U-rib bottom reached yielding strain.

(2) The strain development in the cyclic loading specimens was generally similar to that of the monotonic loading specimen.

(3) The rebars in CA-UHPC specimens did not yield, while those in the NC specimen yielded. This discrepancy arises from the fact that NC loses its ability to withstand tension after cracking, transferring all the tension load to the rebars. Conversely, CA-UHPC maintains its capacity to sustain tension owing to the fiber-bridging effect, thereby delaying the onset of rebar yielding.

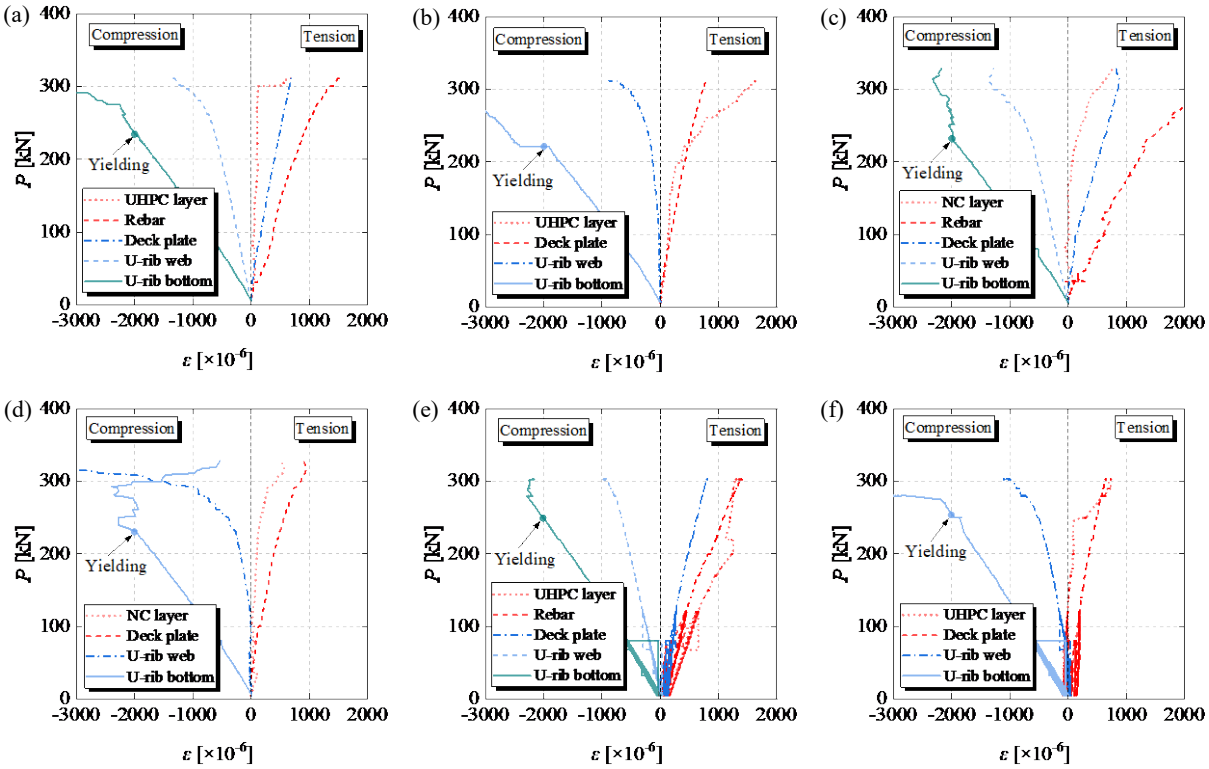

Fig.10. Load-strain curves: (a) SN-3-benchmark at mid-span cross-section; (b) SN-3-benchmark at support cross-section; (c) SN-7-NC at mid-span cross-section; (d) SN-7-NC at support cross-section; (e) SN-8-cyclic at mid-span cross-section; and (f) SN-8-cyclic at support cross-section.

Fig.11 shows the strain distributions along the section height at the mid-span cross-section. In the figure, O_0 and O_{s0} represent the centroid positions of the uncracked steel-concrete composite section (with SN-3 at 287 mm and SN-7 at 279 mm), and of the steel section (including steel rebar and steel plate, with SN-3 and SN-7 both at 234 mm), respectively.

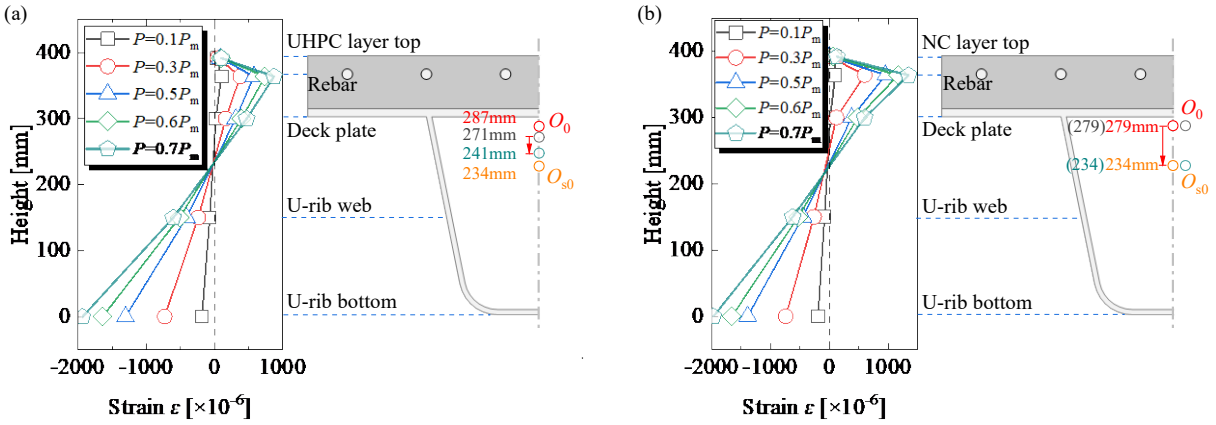

Fig.11. Strain distribution along the section height: (a) SN-3-benchmark; and (b) SN-7-NC.

It can be observed that:

As the load increased from $0.1P_m$ to $0.7P_m$, the strain distribution along the height direction followed a linear pattern (neglecting the concrete strains considering the significant scatter caused by concrete cracking). This indicated that the strain distribution conformed to the plane section assumption, and the arrangement of weld studs in the study can achieve a sound connection between the concrete overlay and the steel plate.

For the CA-UHPC specimen, as the load increased from $0.1P_m$ to $0.7P_m$, the neutral axis of the composite section obtained based on the strain distribution gradually decreased from 271 mm to 241 mm, approaching the centroid location of the steel section (234 mm). Similarly, the neutral axis of the corresponding NC specimen dropped from 279 mm to 234 mm. This demonstrated that CA-UHPC still contributes flexural stiffness to the composite section even after cracking compared to NC.

3. Cracking behavior of CA-UHPC overlay

3.1 Crack patterns

No cracks at the concrete overlays were observed prior to the enforcement of external loads. Fig.12 plots the overall crack distribution at the concrete top surface corresponding to the yielding point. In the figure, "cr+No." represents the main crack numbers, but does not indicate the emerging sequences. It was shown that:

(1) The rebar-reinforced CA-UHPC (R-CA-UHPC) overlays presented similar crack patterns, with uniformly distributed main cracks and densely distributed secondary cracks. Only three localized cracks developed at the CA-UHPC overlay without steel rebars. This

indicated that steel rebars are conducive to the transfer of tensile stress in the CA-UHPC overlay, preventing crack localization.

(2) The rebar-reinforced NC (R-NC) overlay displayed prominent primary cracks that fully penetrated in the transverse direction. Notably, there were no secondary cracks observed in the R-NC overlay. The different crack patterns observed between NC and CA-UHPC can be attributed to the fiber-bridging effect, which facilitates transferring tensile stress from local matrix cracks to the surrounding areas.

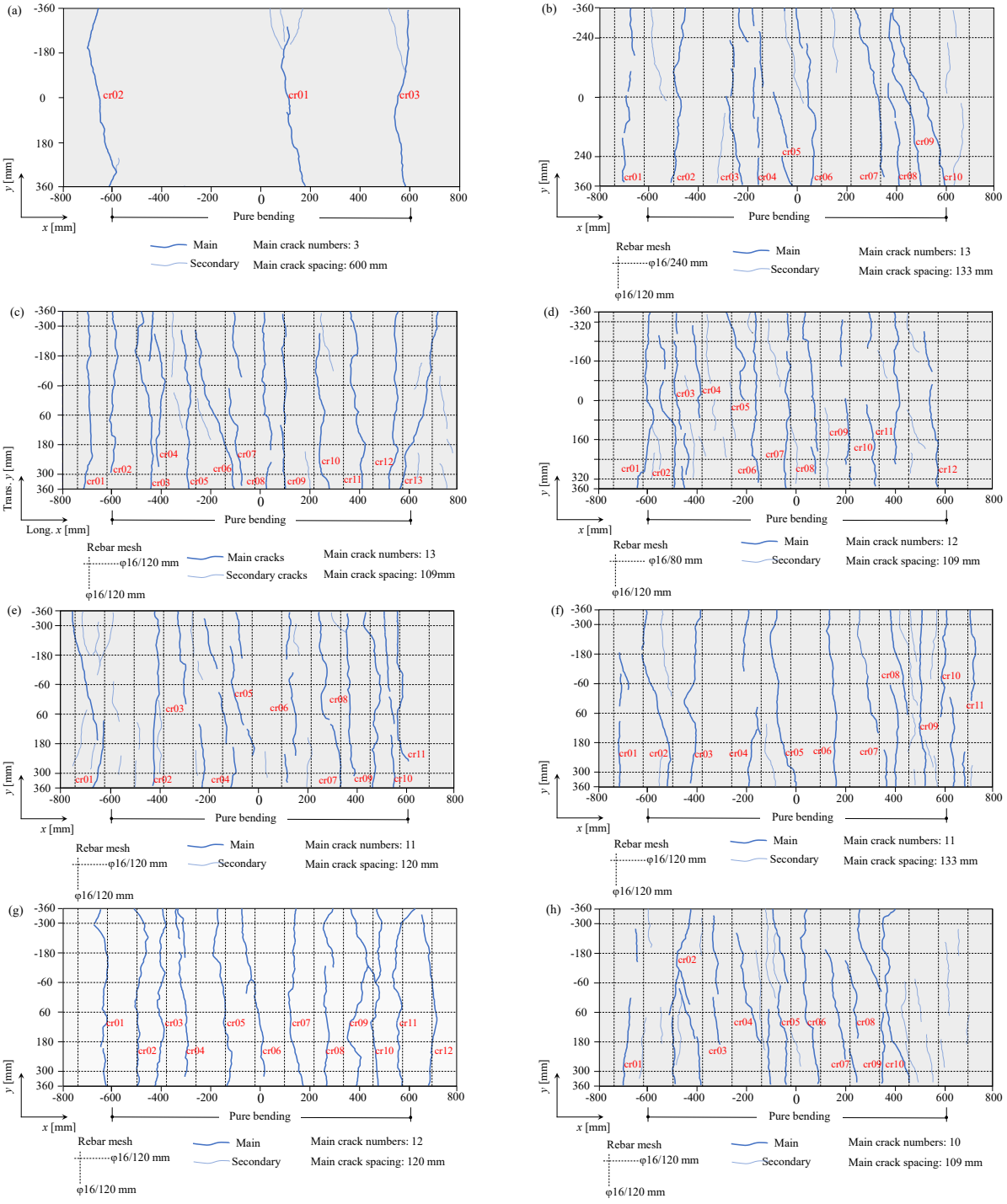

Fig.12. Global crack patterns of the concrete overlays: (a) SN-1, no rebar; (b) SN-2, ρ_s=1.1%, c=20 mm; (c) SN-3-benchmark, ρ_s=2.1%, c=20 mm; (d) SN-4, ρ_s=3.1%, c=20 mm; (e) SN-5,

ρ_s=2.1%, c=10 mm; (f) SN-6, ρ_s=2.1%, c=30 mm; (g) SN-7, NC; and (h) SN-8, cyclic loading.

Fig.13 shows the local crack patterns of the concrete overlays. The R-NC overlay exhibited a single localized feature with clear outlines. By comparison, the CA-UHPC overlay performed a single crack accompanied by locally distributed micro-cracks, resulting in a more dispersed crack outline and difficulties in crack width measurement. Moreover, the local crack pattern of the R-CA-UHPC overlay can be further subdivided into two types. One exhibited a "river bifurcation" characteristic, where one main crack was bifurcated into 2~3 fine cracks, as shown in Fig.13(c). The other was characterized by the smeared crack band composed of multiple fine cracks, as plotted in Fig.13(d). The distinctive crack features in the R-CA-UHPC overlay were owing to the reinforcement-induced (including steel fibers as well as steel rebars) stress redistribution in the CA-UHPC matrix.

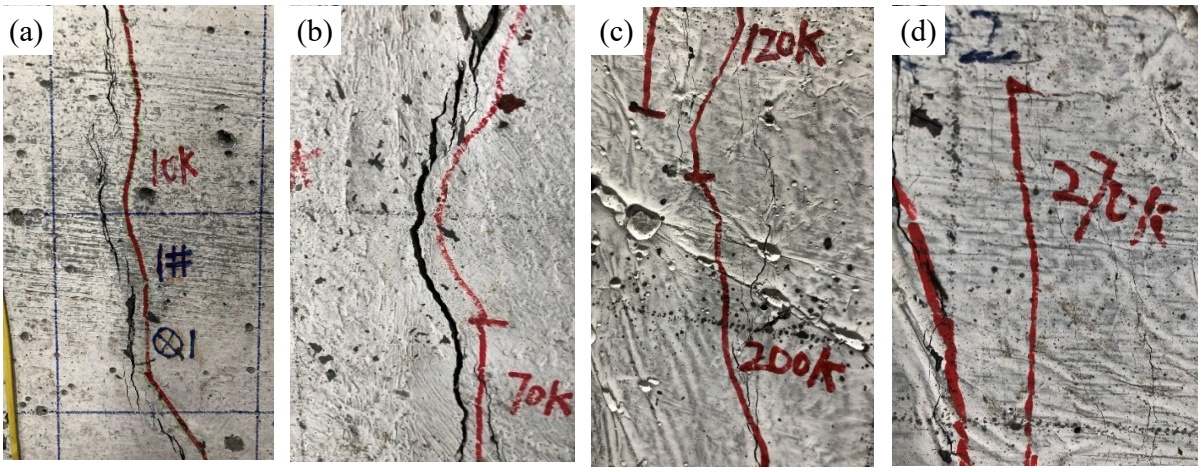

Fig.13. Local crack patterns of the concrete overlays: (a) CA-UHPC without rebar; (b) R-NC; (c) bifurcation feature for R-CA-UHPC; and (d) smeared feature for R-CA-UHPC.

Fig.14 compares the average main crack spacing. Due to the random steel fiber orientations and distributions, the main cracks of the R-CA-UHPC overlay were stochastically distributed. Therefore, the selecting criteria for determining the main cracks were set as: (1) locating at the pure bending zone; (2) exhibiting stable crack width widening; (3) for bifurcation cracks or smeared cracks, only the main crack was considered and the corresponding crack width should be greater than or equal to 0.05 mm.

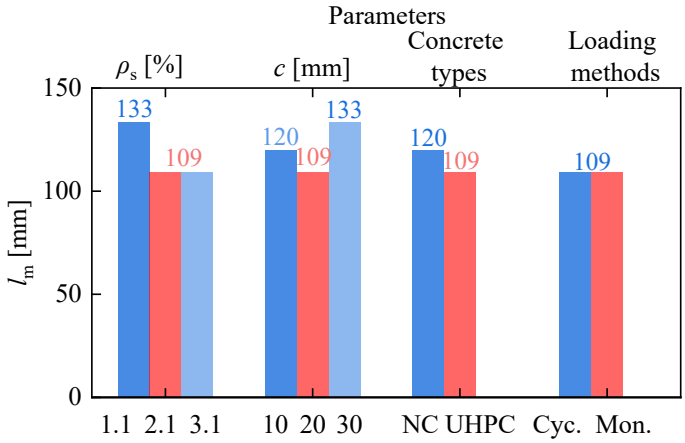

Fig.14. Comparison of average main crack spacing.

As the reinforcement ratio increased, the average main crack spacing tended to decrease. This can be explained by enhancing the reinforcement ratio helped reduce stress transfer length between cracks. However, specimens with reinforcement ratios of 2.1% and 3.1% had the same average main crack spacing of 109 mm, which may be influenced by factors such as fiber distributions, shrinkage, and creep. The average main crack spacing increased with the concrete cover, indicating a weakened constraint effect of steel rebars on the concrete top surface. The influences of reinforcement ratio and concrete cover on the average main crack spacing of CA-UHPC overlays are consistent with the conclusions obtained in previous studies [28,29].

The average main crack spacing of CA-UHPC was relatively smaller than that of NC, as mentioned earlier, due to the stress transfer by steel fibers. Moreover, cyclic loading had a negligible effect on the average main crack spacing of the CA-UHPC overlay. Furthermore, the average main crack spacing obtained in this experiment ranged from 109 to 133 mm, which was close to the spacing of transverse rebars (120 mm). Although the transverse rebars were placed below the longitudinal rebars in the study, it cannot be denied that the average crack spacing was also affected by the transverse rebar arrangement. Some scholars [30] have pointed out that the cracking of concrete bridge decks in steel-concrete composite beams primarily occurred at the position of transverse rebars. In their experiments, the transverse rebars were arranged closer to the tensile edge of the concrete deck than the longitudinal rebars.

3.2 Load-maximum crack width responses

Fig.15 compares the load-maximum crack width responses for specimens with different parameters. It can be observed that:

(1) the crack width of reinforced specimens was significantly smaller than that of unreinforced specimens. With an increase in reinforcement ratio (with the same concrete cover), the maximum crack width gradually decreased.

(2) The maximum crack width increased along with the concrete cover due to the weakened restraint effect of rebar on cracks. When reinforcement ratios exceed 2.1%,

maximum crack widths of CA-UHPC remain below 0.2 mm prior to U-rib yielding. (3) Under the same load (with the same reinforcement ratio and concrete cover), the maximum crack width of CA-UHPC was close to that of NC. (4) There was no significant difference in the maximum crack width development at cyclic tension compared to monotonic tension.

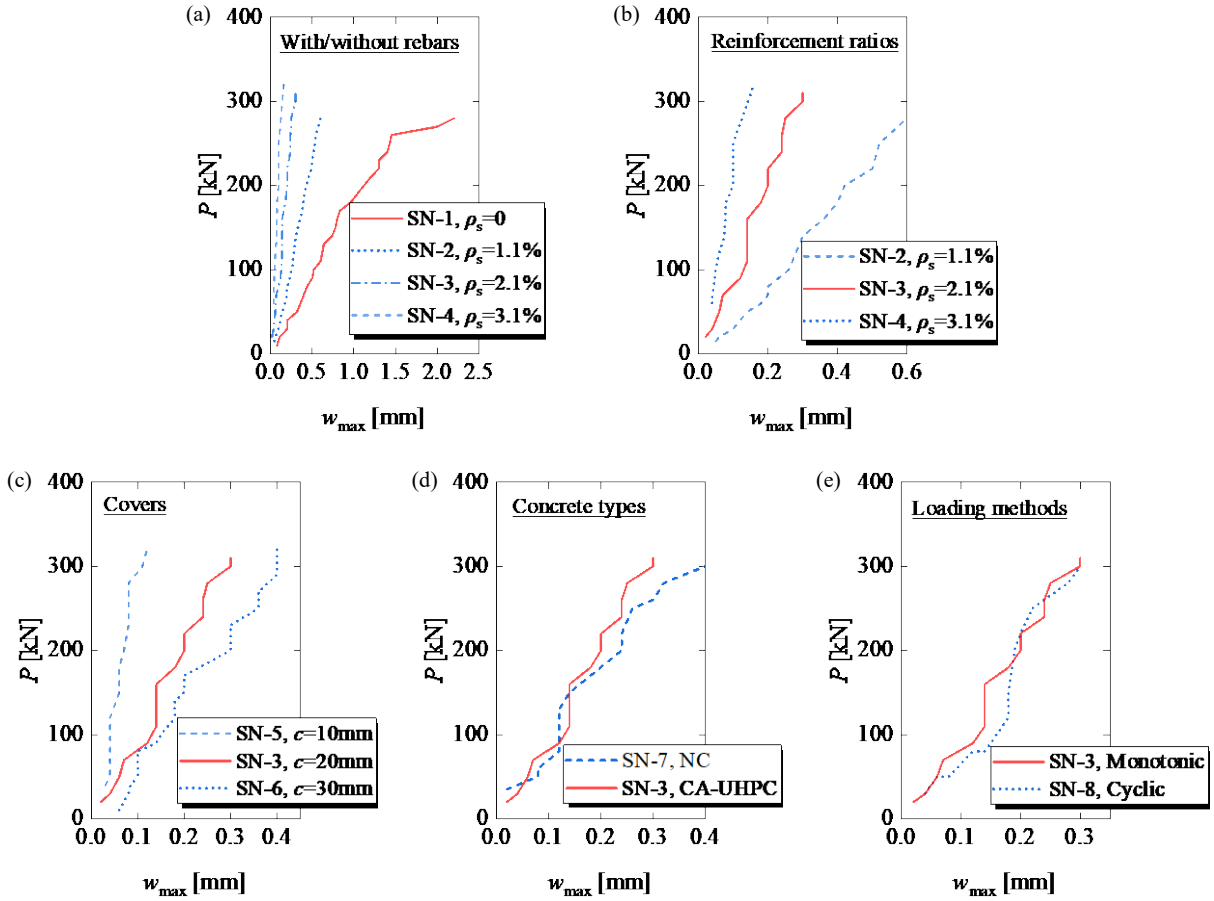

Fig.15. Comparison of load-maximum crack width responses.

3.2.1 Parameter: reinforcement ratios and concrete covers

Fig.16(a) compares the loads at characteristic maximum crack widths regarding reinforcement ratios and concrete covers. The loads for specimens with reinforcement ratios of 3.1%, 2.1%, and 1.1% were 13 times, 6 times, and 3 times the load of the unreinforced specimen, respectively. This indicated that increasing the reinforcement ratios significantly helps control the crack widths in the CA-UHPC overlay.

As the concrete cover decreased successively from 30 mm to 20 mm and 10 mm, the loads at maximum crack width of 0.1 mm increased by 80% and 486%, respectively. It was demonstrated that reducing the concrete cover contributes to restraining crack development.

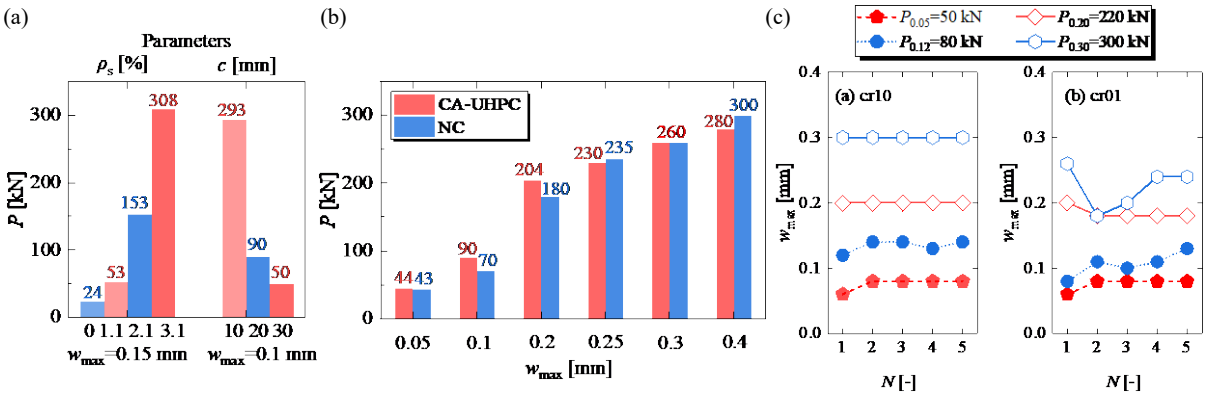

Fig.16. Investigated parameters analysis: (a) influence of reinforcement ratios and concrete covers on characteristic loads; (b) influence of concrete types on characteristic loads; and (c) maximum crack width-cyclic number relationships at the peak loads.

3.2.2 Parameter: concrete types

Fig.16(b) shows the load comparison between NC and CA-UHPC specimens at the same maximum crack widths. Notably, the disparity in loads appeared negligible. Moreover, Fig.17 presents statistics on crack widths when the maximum crack width reaches 0.3 mm. The NC specimen exhibited 8 cracks with widths equal to or exceeding 0.2 mm, whereas the CA-UHPC specimen had only 2 such cracks. Considering both the loads and the overall number of cracks at characteristic widths, it becomes evident that CA-UHPC demonstrated significantly superior crack resistance compared to NC.

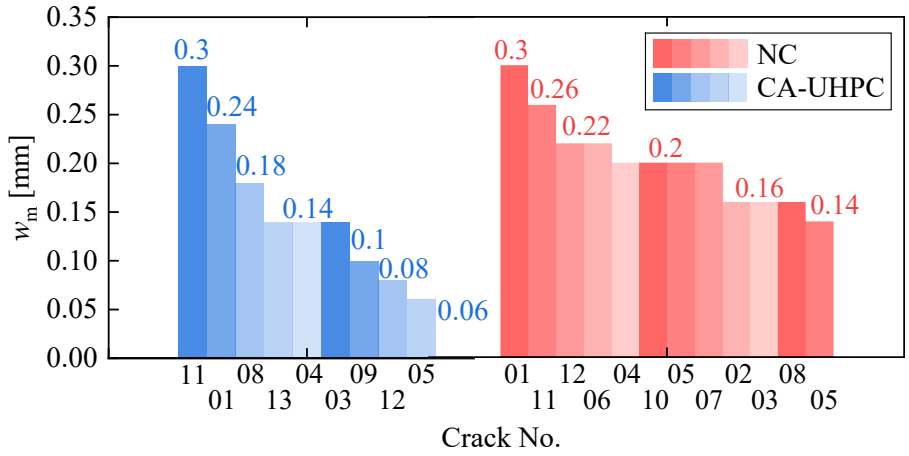

Fig.17. Crack statistics at a maximum crack width of 0.3 mm.

3.2.3 Parameter: loading methods

Fig.16(c) plots the maximum crack width against cyclic numbers at the peak load for cracks cr10 and cr01. It is clear that despite undergoing cyclic unloading and reloading, the maximum crack width at the peak load remained nearly constant. This suggests that finite cyclic loading-unloading has a negligible effect on the maximum crack width.

3.3 Load-rebar strain responses

Rebar strain can serve as an indirect indicator of the cracking behavior of reinforced concrete elements. Fig.18(a) compares the load-rebar strain curves of the tested specimens. In CA-UHPC specimens, the development of rebar strain remained relatively consistent with increasing loads, and the rebar did not yield. As for the NC specimen, the rebar strain demonstrated multiple instances of rebound owing to the cracking instability of NC. Moreover, the rebar yielded prior to reaching the peak load, indicating a more substantial involvement of rebar in tension in NC.

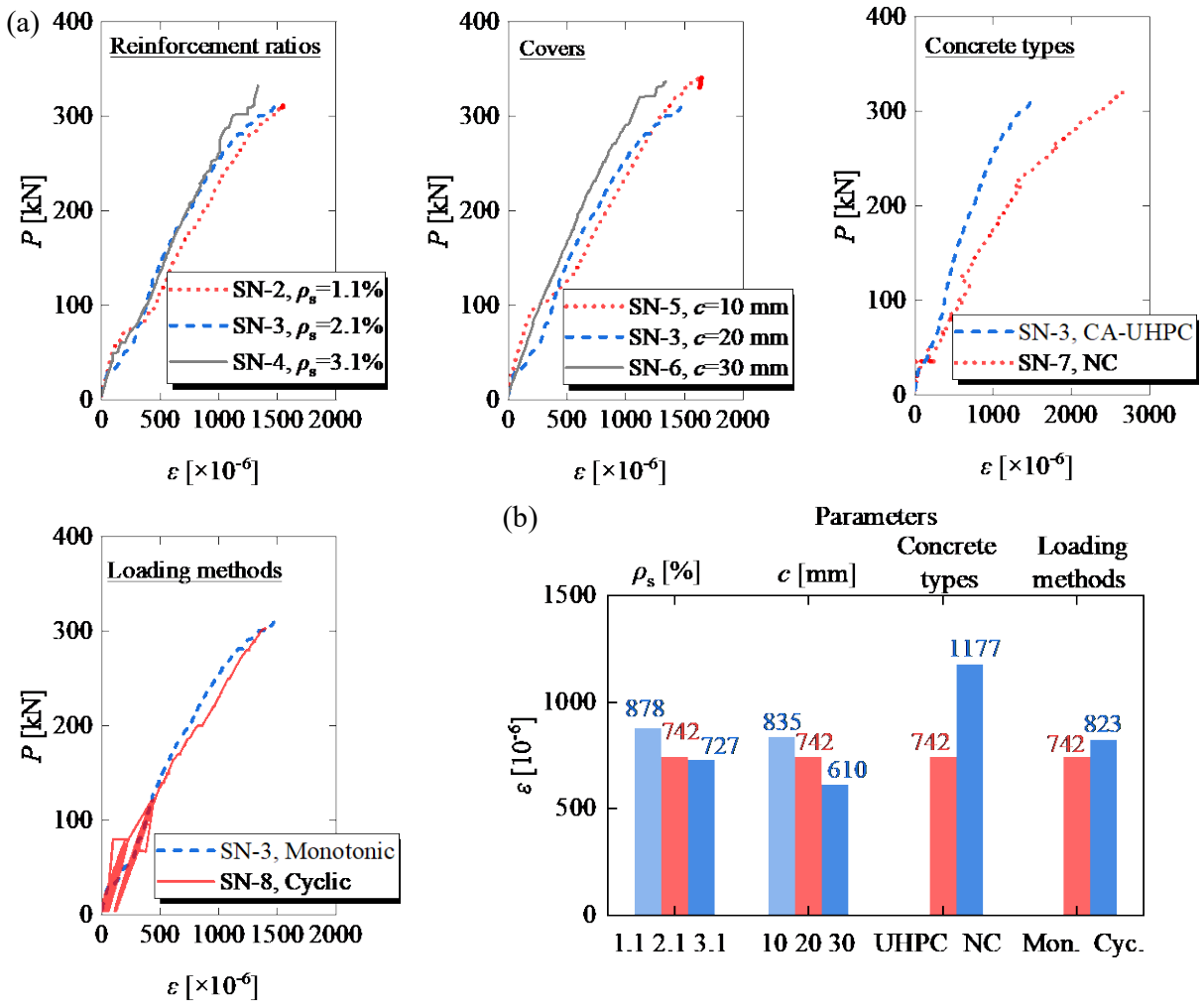

Fig.18. Comparisons of investigated parameters on: (a) load-rebar strain curves; and (b) rebar strain at P=200 kN.

Fig.18(b) illustrates the rebar strain comparison at P=200 kN (approximately corresponding to the yielding at the U-rib bottom). It can be observed that:

(1) Appropriately increasing the reinforcement ratio can reduce the rebar strain, mitigating the role of single reinforcement in restraining crack propagation.

(2) Increasing the concrete cover leads to the rebar closer to the neutral axis of the composite section, resulting in smaller strain and a corresponding weakening of its role in restraining crack development.

(3) The rebar strain in NC specimens was approximately 1.6 times that of the CA-UHPC specimens, indicating once again that NC contributes less to tensile resistance, and CA-UHPC can still provide excellent tensile resistance after cracking.

(4) Under cyclic loading, the rebar strain was slightly higher than that under monotonic loading, indicating the influence of the loading method was insignificant.

4. Restrained shrinkage effect analysis

4.1 Restrained shrinkage effect

Fig.19 presents the schematic restrained shrinkage effect in the steel-UHPC composite deck. When casting UHPC overlay on the steel deck, the free shrinkage of UHPC is restrained by the steel deck as well as the embedded steel rebar. It should be noted that UHPC exhibits extremely high autogenous shrinkage but insignificant drying shrinkage at early ages, owing to a low w/b ratio and high fineness of its constituents [14,16]. Consequently, initial restrained tensile stress $\sigma_{ct,re0}$ develops in the UHPC. Moreover, the developed shrinkage deformation is further decreased due to the tensile creep properties of concrete material. The restrained shrinkage and tensile creep continue to develop over time, leading to the final restrained tensile stress $\sigma_{ct,re}$ and final restrained shrinkage strain $\varepsilon_{cs,re}$ in the UHPC overlay. This mechanism provides a good explanation for the premature cracking of the CA-UHPC overlay stated in sec 2.2.2.

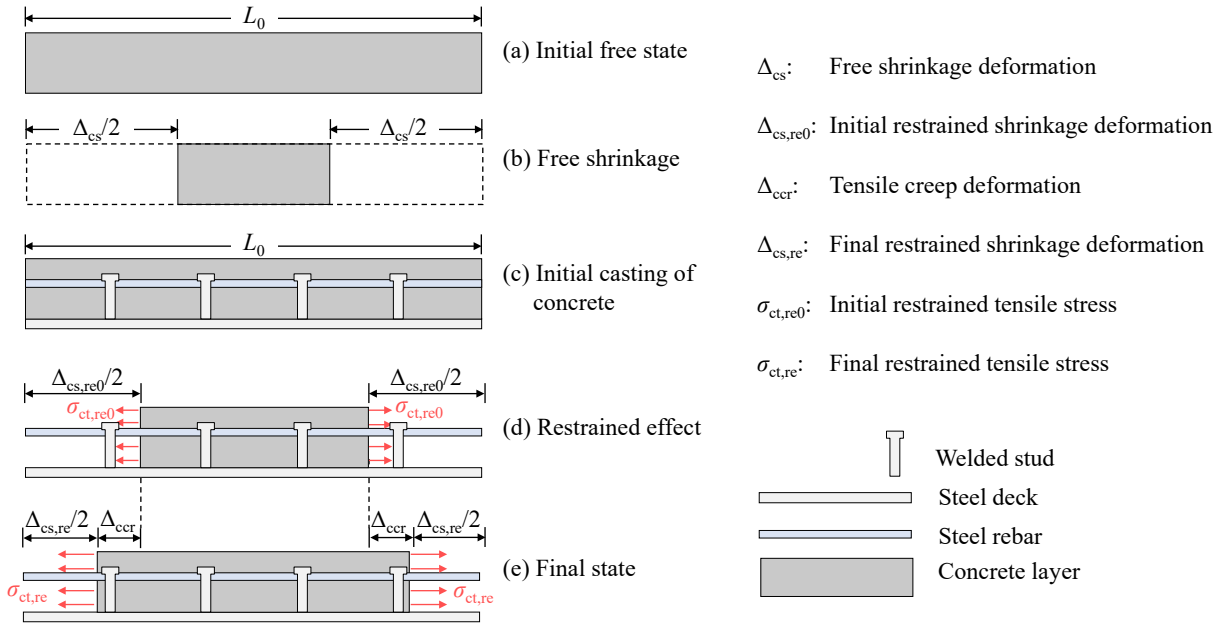

Fig.19. Schematic restrained shrinkage effect.

4.2 Theoretical derivation

To quantify the influence of the restrained shrinkage effect on the internal force redistribution in the tested specimens, theoretical derivation was conducted based on the

Trost-Bazant algebraic equations [31]. The lower-depth CA-UHPC overlay withstands stronger restraint from the steel deck compared with the upper overlay, therefore the non-uniform shrinkage develops over the CA-UHPC depth, as plotted in Fig.20. Considering the CA-UHPC overlay has a thick depth of 80 mm, a uniform shrinkage was assumed in the theoretical analysis. Additionally, the analysis exclusively addressed the impact of restrained shrinkage on axial strain, with the effect on cross-sectional curvature neglected.

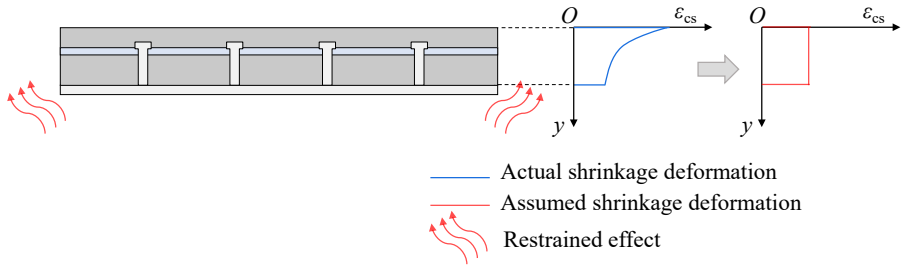

Fig.20. Assumend shrinkage profile over the depth.

Fig.21 illustrates the schematic restrained-shrinkage-effect-induced internal force redistributions in a composite bridge deck, where O_c and O_{s0} represent the centroids of the CA-UHPC overlay and the steel component (including steel plates and rebars) respectively, and y_{sc} denotes the vertical distance between the two centroids. The cross-sectional area, moment of inertia, and elastic modulus for the concrete overlay are denoted as A_c, I_c, and E_c, respectively, while those of the steel component are marked as A_s, I_s, and E_s, respectively.

At the onset of the steel-concrete composite interaction, denoted as time t_0, the curvature of the cross-section is $\kappa(t_0)$, and the initial axial force and bending moment carried by the CA-UHPC overlay are denoted as $N_c(t_0)$ and $M_c(t_0)$ respectively, while that borne by the steel component is marked as $N_s(t_0)$ and $M_s(t_0)$ respectively. At this moment, the axial force and bending moment of the composite section are represented as $N(t_0)$ and $M(t_0)$ respectively, and their relations can be expressed as:

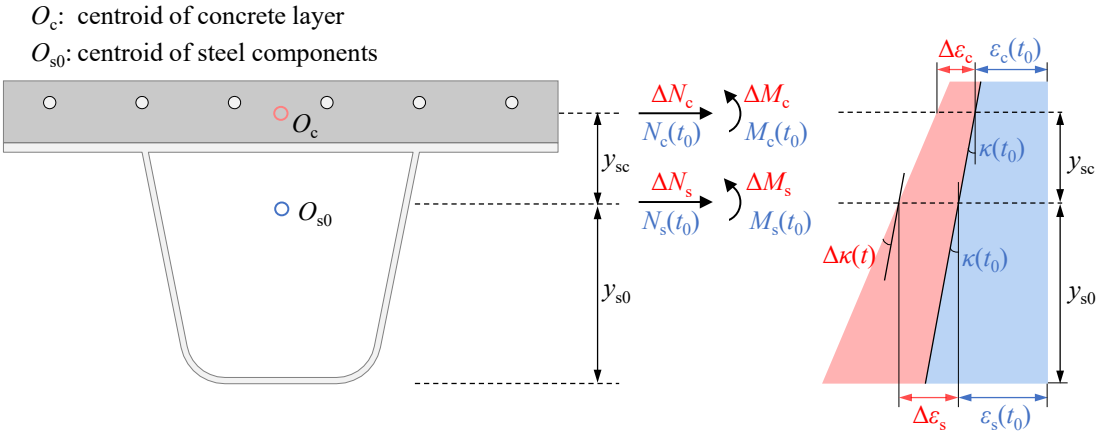

Fig.21. Schematic internal force redistributions in composite bridge deck induced by restrained shrinkage effect.

$$N_c(t_0) + N_s(t_0) = N(t_0) \tag{3}$$

$$M_c(t_0) + M_s(t_0) + N_s(t_0) \cdot y_{sc} = M(t_0) \tag{4}$$

As curing time progresses from t_0 to t, the internal forces distribution develops in the composite section due to the restrained shrinkage effect. Consequently, $N_c(t_0)$, $M_c(t_0)$, $N_s(t_0)$, and $M_s(t_0)$ become $N_c(t)$, $M_c(t)$, $N_s(t)$, and $M_s(t)$, respectively. However, the axial force and bending moment of the composite section remain unchanged. Therefore, the expression below is derived:

$$\Delta N_c(t,t_0) + \Delta N_s(t,t_0) = 0 \tag{5}$$

$$\Delta M_c(t,t_0) + \Delta M_s(t,t_0) + \Delta N_s(t,t_0) \cdot y_{sc} = 0 \tag{6}$$

where:

$$\begin{aligned} \Delta N_c(t,t_0) &= N_c(t) - N_c(t_0) \\ \Delta N_s(t,t_0) &= N_s(t) - N_s(t_0) \\ \Delta M_c(t,t_0) &= M_c(t) - M_c(t_0) \\ \Delta M_s(t,t_0) &= M_s(t) - M_s(t_0) \end{aligned} \tag{7}$$

The specimens were not subjected to external loads at the curing stage. The self-weight of the steel plates, rebars, and CA-UHPC overlays were carried by the steel structures. The self-weight can be neglected due to its relatively small effect. Therefore, $N(t_0)$, $N_c(t_0)$, $N_s(t_0)$, $M(t_0)$, $M_c(t_0)$, and $M_s(t_0)$ are all equal to 0. Hence, the following equations can be derived:

$$N_c(t) + N_s(t) = 0 \tag{8}$$

$$M_c(t) + M_s(t) + N_s(t) \cdot y_{sc} = 0 \tag{9}$$

According to the Trost-Bazant method, the algebraic equation represents the relationship between the strain increment induced by shrinkage and creep and the stress increment in concrete, as given by:

$$\Delta\varepsilon_c(t,t_0) = \frac{\sigma_c(t_0)}{E_c} \cdot \varphi(t,t_0) + \frac{\Delta\sigma_c(t,t_0)}{E_c} \cdot \left[1 + \chi(t,t_0) \cdot \varphi(t,t_0)\right] + \varepsilon_{cs}(t,t_0) \tag{10}$$

where: $\sigma_c(t_0)$ is the concrete stress at time t_0; $\Delta\sigma_c(t,t_0)$ is the stress increment of concrete from t_0 to t; $\chi(t,t_0)$ is the aging coefficient for concrete, a parameter less than 1.0; $\varphi(t,t_0)$ is the creep coefficient for concrete; $\varepsilon_{cs}(t, t_0)$ is the free shrinkage strain.

As demonstrated in Sec.2.2.3, the designed stud arrangement ensures a perfect connection between the steel component and the CA-UHPC overlay. Therefore, two deformation compatibility conditions are satisfied:

(1) The strain increment of CA-UHPC overlay at the centroid of the steel component should be equal to the strain increment of steel;

(2) The curvature increment of the CA-UHPC overlay should be equal to that of the steel component.

These conditions can be expressed as:

$$\Delta\varepsilon_{cN}(t,t_0) + \Delta\varepsilon_{cM}(t,t_0) + \varepsilon_{cs}(t,t_0) = \Delta\varepsilon_s(t,t_0) \tag{11}$$

$$\Delta\kappa_c(t,t_0)=\Delta\kappa_s(t,t_0) \tag{12}$$

The Trost-Bazant-algebraic-equation-based deformation compatibility equations are given as:

$$\frac{N_c(t)\left[1+\chi(t,t_0)\cdot\varphi(t,t_0)\right]}{E_cA_c}+\frac{y_{sc}\cdot M_c(t)\left[1+\chi(t,t_0)\cdot\varphi(t,t_0)\right]}{E_cI_c}+\varepsilon_{cs}(t,t_0)=\frac{N_s(t)}{E_sA_s} \tag{13}$$

$$\frac{M_c(t)\left[1+\chi(t,t_0)\cdot\varphi(t,t_0)\right]}{E_cI_c}=\frac{M_s(t)}{E_sI_s} \tag{14}$$

From Eq.(9), $M_s(t)$=- ($M_c(t)$+ $N_s(t)y_{sc}$)= $N_c(t)y_{sc}$- $M_c(t)$ was obtained. Substituting it into Eq.(14), gives the bending moment of the CA-UHPC overlay at time *t*:

$$M_c(t)=\frac{N_c(t)\cdot y_{sc}\cdot E_cI_c}{\left[1+\chi(t,t_0)\cdot\varphi(t,t_0)\right]E_sI_s+E_cI_c} \tag{15}$$

Substituting Eq.(15) into Eq.(13), gives the axial force of the CA-UHPC overlay at time *t*:

$$N_c(t)=\frac{-\varepsilon_{cs}(t,t_0)}{\frac{1+\chi(t,t_0)\cdot\varphi(t,t_0)}{E_cA_c}+\frac{\left[1+\chi(t,t_0)\cdot\varphi(t,t_0)\right]y_{sc}^2}{\left[1+\chi(t,t_0)\cdot\varphi(t,t_0)\right]E_sI_s+E_cI_c}+\frac{1}{E_sA_s}} \tag{16}$$

Hence, the restrained tensile stress generated in the CA-UHPC overlay can be expressed as:

$$\sigma_{ct,re}(t)=\frac{N_c(t)}{A_c}\pm\frac{M_c(t)\cdot y_c}{I_c} \tag{17}$$

Where: y_c is the vertical distance from any point in the CA-UHPC overlay to its neutral axis.

4.3 Discussions and verification

It should be noted that the Trost-Bazant algebraic equation is suitable for predicting long-term strain and stress increments caused by shrinkage and creep (long-term performance) in NC structural elements. Consequently, the elastic modulus of concrete E_c in the equation is commonly assumed to remain constant under standard curing for 28 days. Moreover, given the progressive aging of concrete during service life, the aging coefficient $\chi(t,t_0)$ typically tends to be less than 1. Furthermore, the tension capacity of NC is often disregarded, resulting in the adoption of compressive creep coefficient $\varphi(t,t_0)$.

Compared with conventional NC structural members, the investigated steel-CA-UHPC composite bridge deck has distinct characteristics as follows:

(1) The shrinkage observed in CA-UHPC during the curing stage is predominantly autogenous shrinkage, rather than long-term drying shrinkage. Throughout this period, the elastic modulus of CA-UHPC evolves continuously with age, leading to a non-constant elastic modulus.

(2) During the curing stages, CA-UHPC remains in a state of fresh concrete, thus the

consideration of aging characteristics is unnecessary.

(3) Creep refers to the tensile creep due to the restrained tensile stress.

The basic parameters in Eq.(16) can be obtained:

Parameter 1: The initial interactive time t_0 for steel and CA-UHPC was taken as 0.5d (half a day)，according to the firth author's previous study [32]. The end of curing time t was 37 days.

Parameter 2: Elastic modulus E_c was taken as the equivalent average elastic modulus $E_{c,eq}$ at the curing stage [32], $E_{c,eq}$=0.962$E_{c,28}$, where $E_{c,28}$ is the elastic modulus under standard curing for 28 days. Here, $E_{c,28}$ was taken from Table 3. The definition of equivalent average elastic modulus is shown in Fig.22(a).

Parameter 3: Free shrinkage $\varepsilon_{cs}(t, t_0)$ was taken as -681με [32], shown in Fig.22(b).

Parameter 4: Tensile creep coefficient $\varphi(t,t_0)$ was taken as 3.629 [32], shown in Fig.22(c).

Parameter 5: Aging coefficient $\chi(t,t_0)$ was assumed to be 1.0 considering without aging process at the curing stage.

Substituting the parameters 1~5 into Eq.s(15)~(17), the theoretical restrained tensile stresses can be obtained.

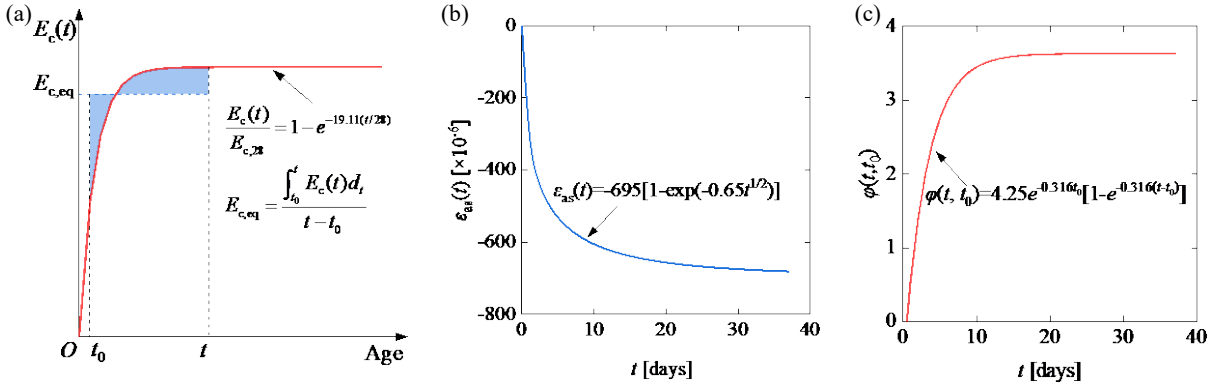

Fig.22. Time-dependent models for CA-UHPC [32]: (a) elastic modulus; (b) autogenous shrinkage; and (c) Tensile creep coefficient.

According to Eq.(2) and the measured initial cracking load P_{cr} listed in Table 7, the initial cracking strength of the CA-UHPC overlay is given:

$$f_{cr}=\frac{P_{cr}L_0y_{c0}}{\alpha_E I_0} \tag{18}$$

Therefore, the experiment-based restrained tensile stress can be calculated as:

$$\sigma_{ct,re}=f_{ct}-f_{cr} \tag{19}$$

The restrained tensile stress distribution over the depth is plotted in Fig.23. Fig.24(a) compares the theoretical and experimental restrained tensile stresses. As indicated, the mean value of the ratio between theoretical and experimental restrained tensile stresses was 1.10, with a coefficient of variation of 23%, thereby confirming the validity of the theoretical derivation.

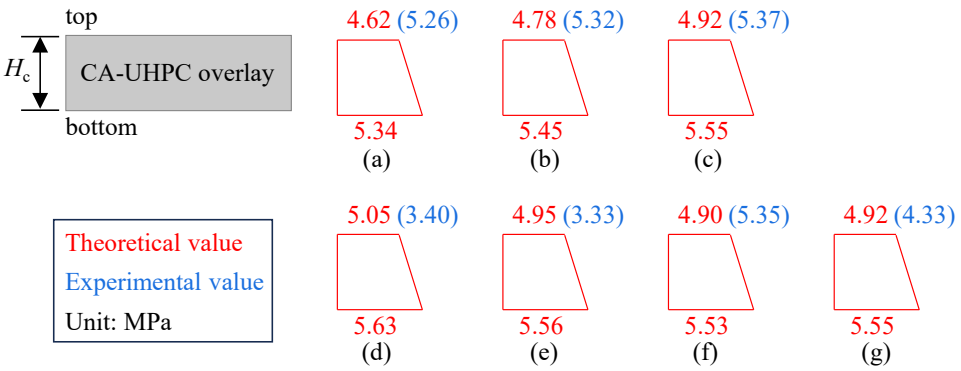

Fig.23. Restrained tensile stress distribution over the depth: (a) SN-1, no rebar; (b) SN-2, ρ_s=1.1%, c=20 mm; (c) SN-3-benchmark, ρ_s=2.1%, c=20 mm; (d) SN-4, ρ_s=3.1%, c=20 mm; (e) SN-5, ρ_s=2.1%, c=10 mm; (f) SN-6, ρ_s=2.1%, c=30 mm; and (g) SN-8, ρ_s=2.1%, c=20 mm, cyclic loading.

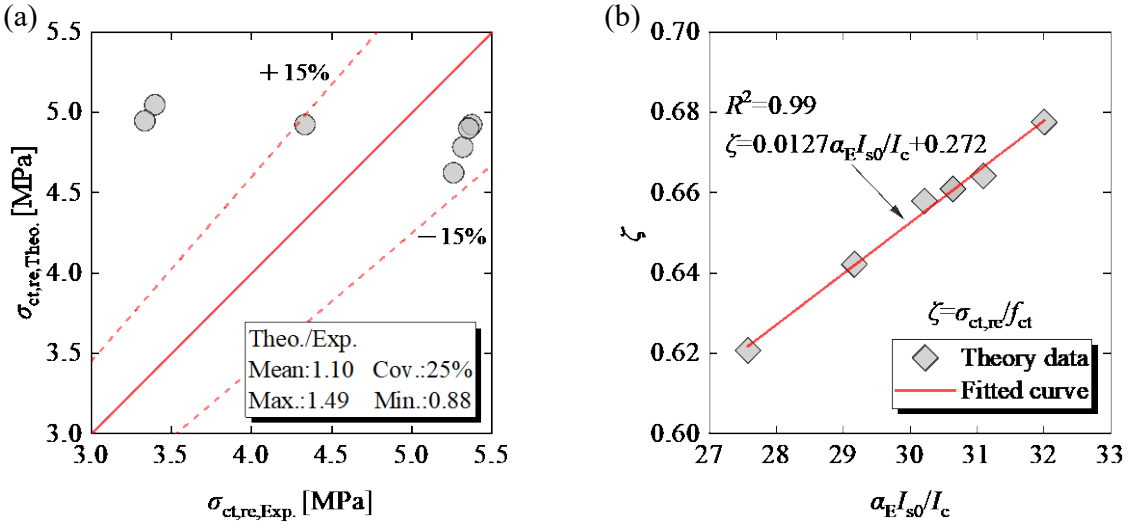

Fig.24. Theoretical analysis: (a) comparison between experimental and theoretical restrained tensile stresses; (b) fitted relation between restrained degree and steel-concrete bending stiffness ratio.

To further quantify and predict the restrained effect of the composite deck, the concept of restrained degree ζ, which was defined as the ratio of restrained tensile stress (theoretical values) to the tensile strength of concrete was proposed, as expressed below.

$$\zeta = \frac{\sigma_{ct,re}}{f_{ct}} \tag{19}$$

The relationship between the restrained degree ζ and the ratio of steel-concrete bending stiffness $\alpha_E I_{s0}/I_c$ was formulated and illustrated in Fig.24(b). A fitted function, denoted as the restrained shrinkage model and described by Eq.(20), was derived for this purpose. Given the specified material properties (E_s, E_c, and f_{ct}) and geometric properties (I_{s0} and I_c), the restrained shrinkage model can be applied to predict the restrained tensile stresses and the initial cracking loads of the composite deck.

$$\zeta = 0.0127\alpha_{\mathrm{E}} I_{\mathrm{s0}} / I_{\mathrm{c}} + 0.272 \tag{20}$$

5. Conclusions

Based on the above investigations, the main conclusions are:

(1) The flexural-tension behavior of steel-concrete composite decks is characterized by four distinct stages: elastic response, concrete cracking, U-rib yielding and buckling, and ultimate failure. Notably, the yielding of U-ribs, rather than concrete cracking, significantly contributes to stiffness reduction. Furthermore, the buckling of U-ribs at support sections determines the load-bearing capacity of the composite deck.

(2) The synergistic reinforcement of steel fibers and steel rebars in the R-CA-UHPC overlay promotes the formation of uniform global crack patterns and distinctive local crack distributions characterized by river bifurcation or crack bands. Conversely, the R-NC overlay displays prominent main cracks with well-defined outlines. Additionally, while steel rebars in the NC overlay undergo yielding, those in the CA-UHPC overlay remain unyielded.

(3) Increasing reinforcement ratios or reducing concrete covers helps to control the maximum crack widths of the CA-UHPC overlay. When reinforcement ratios exceed 2.1%, maximum crack widths of CA-UHPC remain below 0.2 mm prior to U-rib yielding. Limited numbers of cyclic tension yield a negligible impact on crack patterns and maximum crack widths of the CA-UHPC overlay.

(4) The presence of steel plates and rebars restrains the free shrinkage of the CA-UHPC overlay, resulting in restrained tensile stress at the curing stage and premature cracking under external loads. The Trost-Bazant-algebraic-equations-based theoretical analysis was conducted to quantify the restrained shrinkage-induced internal force/stress redistributions in the composite section. Subsequently, a restrained shrinkage model was developed to predict both the restrained tensile stresses and the initial cracking loads of the composite deck.

Acknowledgements

The financial support provided by the Fujian Transportation Science and Technology Project (Grant NO.202126) is greatly appreciated by the authors. The first author also acknowledges the financial support of the China Scholarship Council (Grant NO. 202006260216).

References

[1] R. Wolchuk, Lessons from Weld Cracks in Orthotropic Decks on Three European Bridges, J. Struct. Eng. 116 (1990) 75–84. https://doi.org/10.1061/(ASCE)0733-9445(1990)116:1(75).

[2] R. Wolchuk, Steel Orthotropic Decks: Developments in the 1990s, Transportation Research Record 1688 (1999) 30–37. https://doi.org/10.3141/1688-04.

[3] X. Shao, D. Yi, Z. Huang, H. Zhao, B. Chen, M. Liu, Basic Performance of the

Composite Deck System Composed of Orthotropic Steel Deck and Ultrathin RPC Layer, J. Bridge Eng. 18 (2013) 417–428. https://doi.org/10.1061/(ASCE)BE.1943-5592.0000348.
[4] R. Walter, J.F. Olesen, H. Stang, T. Vejrum, Analysis of an Orthotropic Deck Stiffened with a Cement-Based Overlay, J. Bridge Eng. 12 (2007) 350–363. https://doi.org/10.1061/(ASCE)1084-0702(2007)12:3(350).
[5] S. Teixeira De Freitas, H. Kolstein, F. Bijlaard, Fatigue Assessment of Full-Scale Retrofitted Orthotropic Bridge Decks, J. Bridge Eng. 22 (2017) 04017092. https://doi.org/10.1061/(ASCE)BE.1943-5592.0001115.
[6] R. Wolchuk, Structural Behaviour of Surfacings on Steel Orthotropic Decks and Considerations for Practical Design, Structural Engineering International 12 (2002) 124–129. https://doi.org/10.2749/101686602777965586.
[7] P. Buitelaar, R. Braam, N. Kaptijn, Reinforced High Performance Concrete Overlay System for Rehabilitation and Strengthening of Orthotropic Steel bridge decks, in: 2004 Orthotropic Bridge Conference, 2004.
[8] C.H. Ma, P. Deng, T. Matsumoto, Fatigue analysis of a UHPFRC-OSD composite structure considering crack bridging and interfacial bond stiffness degradations, Engineering Structures 249 (2021) 113330.
[9] P. Deng, H. Mi, H. Mitamura, T. Matsumoto, Stress reduction effects of ultra-high performance fiber reinforced concrete overlaid steel bridge deck developed with a new interfacial bond method, Construction and Building Materials 328 (2022) 127104.
[10] L. Dieng, P. Marchand, F. Gomes, C. Tessier, F. Toutlemonde, Use of UHPFRC overlay to reduce stresses in orthotropic steel decks, Journal of Constructional Steel Research 89 (2013) 30–41. https://doi.org/10.1016/j.jcsr.2013.06.006.
[11] J. Cao, X. Shao, L. Deng, Y. Gan, Static and Fatigue Behavior of Short-Headed Studs Embedded in a Thin Ultrahigh-Performance Concrete Layer, J. Bridge Eng. 22 (2017) 04017005. https://doi.org/10.1061/(ASCE)BE.1943-5592.0001031.
[12] Z. Shi, Q. Su, F. Kavoura, M. Veljkovic, Behavior of short-headed stud connectors in orthotropic steel-UHPC composite bridge deck under fatigue loading, International Journal of Fatigue 160 (2022) 106845. https://doi.org/10.1016/j.ijfatigue.2022.106845.
[13] B. Graybeal, E. Brühwiler, B.-S. Kim, F. Toutlemonde, Y.L. Voo, A. Zaghi, International perspective on UHPC in bridge engineering, Journal of Bridge Engineering 25 (2020) 04020094.
[14] D.-Y. Yoo, N. Banthia, Y.-S. Yoon, Effectiveness of shrinkage-reducing admixture in reducing autogenous shrinkage stress of ultra-high-performance fiber-reinforced concrete, Cement and Concrete Composites 64 (2015) 27–36.
[15] T. Xie, C. Fang, M.M. Ali, P. Visintin, Characterizations of autogenous and drying shrinkage of ultra-high performance concrete (UHPC): An experimental study, Cement and Concrete Composites 91 (2018) 156–173.
[16] D.-Y. Yoo, S. Kim, M.-J. Kim, Comparative shrinkage behavior of ultra-high-performance fiber-reinforced concrete under ambient and heat curing conditions, Construction and Building Materials 162 (2018) 406–419.

https://doi.org/10.1016/j.conbuildmat.2017.12.029.
[17] W. Li, Z. Huang, G. Hu, W.H. Duan, S.P. Shah, Early-age shrinkage development of ultra-high-performance concrete under heat curing treatment, Construction and Building Materials 131 (2017) 767–774.
[18] M. Valipour, K.H. Khayat, Coupled effect of shrinkage-mitigating admixtures and saturated lightweight sand on shrinkage of UHPC for overlay applications, Construction and Building Materials 184 (2018) 320–329.
[19] L. Teng, M. Valipour, K.H. Khayat, Design and performance of low shrinkage UHPC for thin bonded bridge deck overlay, Cement and Concrete Composites 118 (2021) 103953.
[20] J. Ma, M. Orgass, F. Dehn, D. Schmidt, N.V. Tue, Comparative investigations on ultra-high performance concrete with and without coarse aggregates, in: International Symposium on Ultra High Performance Concrete, Kassel, Germany, 2004: pp. 205–212.
[21] A. Cwirzen, V. Penttala, C. Vornanen, Reactive powder based concretes: Mechanical properties, durability and hybrid use with OPC, Cement and Concrete Research 38 (2008) 1217–1226. https://doi.org/10.1016/j.cemconres.2008.03.013.
[22] S. Pyo, H.-K. Kim, B.Y. Lee, Effects of coarser fine aggregate on tensile properties of ultra high performance concrete, Cement and Concrete Composites 84 (2017) 28–35. https://doi.org/10.1016/j.cemconcomp.2017.08.014.
[23] J. Liu, F. Han, G. Cui, Q. Zhang, J. Lv, L. Zhang, Z. Yang, Combined effect of coarse aggregate and fiber on tensile behavior of ultra-high performance concrete, Construction and Building Materials 121 (2016) 310–318. https://doi.org/10.1016/j.conbuildmat.2016.05.039.
[24] P. Li, Q. Yu, H. Brouwers, Effect of coarse basalt aggregates on the properties of Ultra-high Performance Concrete (UHPC), Construction and Building Materials 170 (2018) 649–659.
[25] C. Li, B. Chen, J. Wei, Shrinkage and mechanical properties of UHPC with coarse aggregate, Journal of Traffic and Transportation Engineering 19 (2019) 11–20.
[26] Z. Shi, Q. Su, F. Kavoura, M. Veljkovic, Fatigue behavior evaluation of full-scale OSD-UHPC composite bridge deck system, Engineering Structures 275 (2023) 115179. https://doi.org/10.1016/j.engstruct.2022.115179.
[27] Z. Shi, Q. Su, F. Kavoura, M. Veljkovic, Uniaxial tensile response and tensile constitutive model of ultra-high performance concrete containing coarse aggregate (CA-UHPC), Cement and Concrete Composites 136 (2023) 104878. https://doi.org/10.1016/j.cemconcomp.2022.104878.
[28] J. Luo, X. Shao, W. Fan, J. Cao, S. Deng, Flexural cracking behavior and crack width predictions of composite (steel+ UHPC) lightweight deck system, Engineering Structures 194 (2019) 120–137.
[29] M. Qiu, Study on the basic performance and calculation theory of reinforced UHPC members, Doctoral thesis, Hunan University, 2021.
[30] Q. Sun, Y. Yang, J. Fan, Y. Zhang, Y. Bai, Effect of longitudinal reinforcement and prestressing on stiffness of composite beams under hogging moments, Journal of Constructional Steel Research 100 (2014) 1–11.

https://doi.org/10.1016/j.jcsr.2014.04.017.
[31] H. Rüsch, D. Jungwirth, H.K. Hilsdorf, Creep and shrinkage: their effect on the behavior of concrete structures, Springer-Verlag, New York, U.S.A., 2012.
[32] Z. Shi, M. Liang, Q. Su, T. Kanstad, L. Ferrara, Tensile behavior of rebar-reinforced coarse aggregate ultra-high performance concrete (R-CA-UHPC) members: Experiments and restrained shrinkage creep effect, Cement and Concrete Composites (2024, Accepted).